Journal of Materials Chemistry A

Syngas production at a near-unity H_2/CO ratio from photo-thermo-chemical dry reforming of methane on a Pt decorated Al_2O_3-CeO_2 catalyst

Journal:	*Journal of Materials Chemistry A*
Manuscript ID	TA-ART-11-2021-010088.R1
Article Type:	Paper
Date Submitted by the Author:	03-Feb-2022
Complete List of Authors:	Feng, Xuhui; Texas A&M University, J. Mike Walker '66 Department Mechanical Engineering Du, Zichen; Texas A&M University, J. Mike Walker '66 Department Mechanical Engineering Sarnello, Erik; Northern Illinois University, Department of Chemistry and Biochemistry Deng, Wei; Texas A&M University, J. Mike Walker ’66 Department of Mechanical Engineering Petru, Cullen; Texas A&M University, J. Mike Walker ’66 Department of Mechanical Engineering Fang, Lingzhe; Northern Illinois University, Department of Chemistry and Biochemistry Li, Tao; Northern Illinois University, Department of Chemistry and Biochemistry; Argonne National Laboratory Li, Ying; Texas A&M University, J. Mike Walker '66 Department Mechanical Engineering

Syngas production at a near-unity H_2/CO ratio from photo-thermo-chemical dry reforming of methane on a Pt decorated Al_2O_3-CeO_2 catalyst

Xuhui Feng,[a] Zichen Du,[a] Erik Sarnello,[b] Wei Deng,[a] Cullen R. Petru,[a] Lingzhe Fang,[b] Tao Li,[b, c] and Ying Li [a,*]

a. J. Mike Walker '66 Department of Mechanical Engineering, Texas A&M University, College Station, TX 77843 United States

b. Department of Chemistry and Biochemistry, Northern Illinois University, DeKalb, IL 60115 United States

c. X-ray Science Division, Advanced Photon Source, Argonne National Laboratory, Lemont, IL 60439 United States

* Corresponding author: yingli@tamu.edu

Abstract

In this work, a Pt catalyst supported on equimolar Al_2O_3-CeO_2 binary oxide (Pt-Al-Ce) was prepared and applied in photo-thermo-chemical dry reforming of methane (DRM) driven by concentrated solar irradiation. It was found that the Pt-Al-Ce catalyst showed good stability in DRM reactions and significant enhancements in H_2 and CO production rates compared with Pt/CeO_2 (Pt-Ce) and Pt/Al_2O_3 (Pt-Al) catalysts. Under a reaction temperature of 700 ℃ with 30-sun equivalent solar irradiation, the Pt-Al-Ce catalyst exhibits a stable DRM catalytic performance at a H_2 production rate of 657 mmol·g^{-1}·h^{-1} and a CO production rate of 666 mmol·g^{-1}·h^{-1}, with the H_2/CO ratio almost equal to unity. These production rates and the H_2/CO ratio were significantly higher than those obtained in the dark at the same temperature. The light irradiation was found to activate photocatalytic activities on Pt-Al-Ce and reduce the reaction activation energy. *In situ* diffuse reflectance infrared Fourier transform spectroscopy (*in situ* DRIFTS) was applied to identify the active intermediates in the photo-thermo-chemical DRM process, which were bidentate/monodentate carbonate, absorbed CO on Pt, and formate. The benefits of the binary Al_2O_3-CeO_2 substrate could be ascribed to that Al_2O_3 promoted methane dissociation while CeO_2 stabilized and eliminated possible coke formation, leading to high catalytic DRM activity and stability.

1. Introduction

Synthesis gas, or syngas, a mixture of H_2 and CO, is an important material for a number of industrial applications as fuel gas or the raw material for varied chemical synthesis processes.[1] Currently, the most widely used technique for syngas produce is the steam methane reforming (SMR) processes,[2] where water vapor interacts with methane under high temperature and pressure conditions (700-1000 ℃ and 3-25 atm)[3] and produces H_2 and CO. One of the drawbacks of the SMR process is the excessive amount of energy input required for water steam generation and reaction gas compression.[2, 3] The recent research progress has turned the spotlight on a milder syngas production technique, dry reforming of methane (DRM). The DRM process converts the two major greenhouse gases, CO_2 and CH_4 into syngas under the atmospheric pressure and a relatively mild temperature range (650-850 ℃),[4] making it less energy-demanding from the industrial application perspective. DRM has been suggested as an environmental strategy to utilize CO_2 molecules for valuable chemical/fuel production.[5, 6] In addition, DRM makes it possible to directly use the CO_2 impurities that already exist in natural gas,[7] which is particularly favorable for oil field gas that contains a significant concentration of CO_2. The ideal H_2:CO ratio of DRM syngas is 1:1, which fits an industrial hydroformylation process.[8] Despite the advantages of DRM and the reduced energy consumption compared with SMR, a relatively high temperature is still needed to initiate the traditional thermal-driven DRM process,[9-11] which, again, demands extensive energy input.[12, 13] Further innovations to lower the energy demand are necessary.

Recently, our research group introduced a photo-thermo-chemical approach for the DRM process,[14, 15] where concentrated sunlight was applied to partially provide thermal energy and photoactive Pt/CeO_2-based catalysts (Pt decorated Si-doped[14] and Zn-doped CeO_2[15]) were used to make better use of the concentrated sunlight and further improve the DRM performance. The Pt-CeO_2-based catalysts show highly efficient and stable DRM catalyzing capabilities and exhibit substantial DRM reaction rate

enhancements under concentrated sunlight irradiation, compared to those under dark conditions. The Pt-CeO_2-based catalysts convert photon energy into chemical energy through the photo-induced activities on the metal oxide substrate.[14, 16, 17] The high performance and stability of the photo-thermal driven DRM reaction on Pt-CeO_2-based catalysts benefit from both the photoactivity.[16] and the high surface oxygen mobility[18] of the CeO_2 substrate, which also promotes the coke resistance capacity of the catalysts.

In addition to the high energy consumption, another issue involved in the DRM process is the H_2/CO ratio that is lower than 1.0 in the products, which is likely related to a side reaction: reverse water-gas shift (RWGS) reaction ($H_2 + CO_2 \rightarrow H_2O + CO$).[19, 20] DRM process on numbers of noble metal-based catalytic materials, including Ru-based,[21, 22] Pt-based,[15, 23] Rh-based,[24] and Pd-based[25, 26] catalysts, observes deteriorated H_2/CO ratios. For example, Damyanova *et al*.[27] applied a type of Pt/CeO_2-ZrO_2 catalyst for DRM reaction; only a low H_2/CO ratio of 0.51 was observed, which is likely associated with the presence of basic centers on ZrO_2 material.[28] Wysocka *et al*.[29] studied and compared the DRM performance of Ru-Ni/ZrO_2 and Ru-Ni/Al_2O_3 catalysts. However, due to the tendency of Ru catalyst in promoting RWGS reactions,[30] only a H_2/CO ratio of ~0.7 was obtained. Advanced catalyst design is demanded to improve H_2 selectivity in the DRM process.

In efforts to design high H_2/CO ratio generation catalysts, Benrabaa *et al*.[31] recently reported the application of SiO_2 supported nickel ferrite catalysts in the DRM process, where it was demonstrated that H_2/CO production ratio can be promoted by Lewis acidic sites on the catalyst surface. However, Hambali *et al.*[32] later indicated that strong catalyst surface acidity may lead to, despite enhanced H_2 selectivity, catalyst coking, and deactivation. In light of these two studies, it seems that an improved H_2/CO ratio can be achieved by coupling a catalyst with a weak acidic promoter. Al_2O_3, a type of abundant and low-cost chemical compound with intrinsic mild acidic characteristics[33, 34] that has long been in catalyst design in a number of industrial processes including hydrocarbon isomerization,[34] catalytic cracking,[35] etc., can be

an ideal addition on DRM catalysts to improve hydrogen production selectivity in DRM process.

In this work, Pt decorated equimolar Al_2O_3-CeO_2 catalyst was prepared and applied for the photo-thermal driven DRM process. The first objective of this study is to introduce a facile and economic approach in catalyst design to improve the catalytic activity and H_2/CO ratio in the DRM process. Based on the aforementioned literature review, it is expected that Pt/Al_2O_3-CeO_2 material promotes H_2 generation and enhances the H_2/CO ratio in the DRM process catalyzed compared with Pt-CeO_2 based catalyst. Additionally, although alumina has been long applied as a substrate material in DRM process,[36, 37] there are still knowledge gaps regarding the synergetic effects between Al_2O_3 and CeO_2 in photo-driven DRM processes. Therefore, more importantly, the second objective of this work is to investigate the synergetic effects of Al_2O_3 and CeO_2 as substrate in photo-driven DRM process. Thirdly, although a number of studies[14, 15, 38-41] have demonstrated light irradiation promotes DRM performance on photoactive catalysts, the mechanism behind the performance enhancement is still not fully understood. For this reason, the third objective of this work is to uncover the role of light irradiation in the photo-thermo-chemical DRM process.

2. Experimental

2.1 Catalyst preparation

Metal oxide substrates were prepared according to previous reports[14, 15] with minor modifications. To prepare CeO_2 substrate, two solutions were made. Solution A was prepared by dissolving 5 mmol cetyl trimethyl ammonium bromide (CTAB, $C_{19}H_{42}NBr$, high purity, VWR) in 7.9 g reagent alcohol (>96% ethanol, VWR). Solution B was made by mixing 5 mmol cerium nitrate hexahydrate [$Ce(NO_3)_3 \cdot 6H_2O$, 99.99%, BTC] and 5 mmol citric acid ($C_6H_8O_7$, 99.5+%, Alfa Aesar) in 7.9 g reagent alcohol. Solution A and B were then mixed and stirred for 3 h before being placed in an oven maintained at 60 ℃ overnight

to allow the solvent to evaporate. The solidified gel was then calcined in air at 500 ℃ for 5 h. Al_2O_3 substrate was prepared by using 5 mmol aluminum nitrate nonahydrate [$Al(NO_3)_3 \cdot 9H_2O$, ≥98%, Sigma-Aldrich] instead of cerium nitrate hexahydrate to prepare solution B. Al_2O_3-CeO_2 hybrid substrate was prepared by using 5 mmol $Al(NO_3)_3 \cdot 9H_2O$ and 5 mmol $Ce(NO_3)_3 \cdot 6H_2O$ (nominal atomic ratio Al : Ce = 1:1) instead of solely $Ce(NO_3)_3 \cdot 6H_2O$ or $Al(NO_3)_3 \cdot 9H_2O$ to prepare solution B.

A wet impregnation method was applied to deposit 1 wt.% Pt on the metal oxide substrates and prepare the DRM catalysts. 100 mg metal oxide substrate was dispersed in a liquid mixture containing 5 g deionized water, 4 g methanol (CH_4O, >99.98%, VWR), 4 g acetone (C_3H_6O, VWR), and 2.1 mg chloroplatinic acid (H_2PtCl_6, 99.9%, Alfa Aesar, equivalent to 1 mg Pt) in an alumina crucible. The crucible was then placed on a hot plate maintained at 100 ℃, and the suspension was stirred with a magnetic bar to allow the solvent to evaporate. After the evaporation, the solid was collected and calcined in air at 500 ℃ for 2 h. The materials prepared with CeO_2 substrate, Al_2O_3 substrate, and Al_2O_3-CeO_2 hybrid substrate are denoted as Pt-Ce, Pt-Al, and Pt-Al-Ce, respectively.

2.2 Catalyst characterization

X-ray diffraction (XRD) patterns were obtained on a Bruker-AXS D8 advanced Bragg-Brentano X-ray powder diffractometer. Energy-dispersive X-ray spectroscopy (EDS) analysis was conducted with a JEOL JSM-7500F field emission scanning electron microscope (FE-SEM). The morphology of catalyst samples was investigated on a JEOL JEM2100F transmission electron microscope (TEM). X-ray photoelectron spectroscopy analyses were conducted on an Omicron DAR 400 XPS/UPS system. UV-Vis light absorption data were obtained on a Hitachi U-4100 UV-Vis-NIR spectrophotometer.

2.3 Photo-thermal driven DRM performance measurements

The experimental setup of the photo-thermal driven DRM catalyst performance measurements is

similar to that employed in our previous studies.[14, 15] As shown in Figure S1, a ScienceTech solar simulator (operated at 1200W, equivalent to 30-sun irradiation, the light spectrum is shown in Figure S2) was used as the light source. 5 mg catalyst sample was dispersed in 2 ml deionized water to form a catalyst suspension. The suspension was then dripped onto a piece of oval quartz fiber, which was later placed onto an oval catalyst holder. The catalyst holder was then placed into a quartz tube reactor (Figure S1). The position of the catalyst holder was carefully aligned inside the reactor to ensure the thermocouple tip contacts the quartz filter surface and aligns with the centerline of the catalyst holder and the reactor. The tube reactor was heated by a tube furnace, where a window was made to allow sunlight to irradiate on the catalyst. Prior to the performance test, the catalyst was firstly reduced at 700 ℃ by a gas mixture of H_2 (20.2 standard cubic centimeter per minute, or 20.2 sccm) and Ar (43.6 sccm) for 1 h, while two mass flow controllers controlled the gas flow rate. After the reduction process, the furnace was powered off, and the tube reactor was then purged with Ar (150 sccm) to eliminate H_2 in the reactor. After 30 min of Ar purging, the solar simulator was powered on at 1200 W and the tube furnace was turned on and set at a desired reaction temperature while maintaining Ar gas flow. The solar lamp operated at 1200 W alone can only heat up the reactor to ~ 450 ℃. Therefore, auxiliary heating from the furnace is needed. Once the reactor reached the desired reaction temperature, Ar gas was turned off and a premixed gas mixture (10% CH_4, 10% CO_2, balanced Ar, hereinafter referred to as "reaction gas") was introduced into the reactor at a gas flow rate of 12 sccm. The outlet of the reactor is connected to a Shimadzu GC-2014 gas chromatograph to determine the chemical composition of the produced gas. Similar tests were conducted without concentrated solar irradiation.

2.4 *In situ* diffuse reflectance infrared Fourier transform spectroscopy (*in situ* DRIFTS) analyses

A similar setup reported in our previous study was applied to conduct the i*n situ* DRIFTS

analyses.[42] The data acquisition was performed with a Nicolet 6700 spectrometer (Thermo Electron) equipped with a Praying Mantis DRIFTS accessory and a reaction chamber (Harrick Scientific, HVC-DRP). Figure S3 shows the diagram of the *in situ* DRIFTS reaction chamber. The highest temperature the reaction chamber can reach is 600 ℃. Prior to each *in situ* DRIFTS test, the catalyst sample was firstly reduced by a gas mixture of H_2 (20.2 sccm) and Ar (43.6 sccm) for 15 min at 600 ℃ in the DRIFTS reaction chamber. After the reduction process, H_2 gas flow was turned off and the reaction chamber was allowed to cool down naturally to the target testing temperature while Ar protected the catalyst sample at a flow rate of 43.6 sccm. Once the DRIFT chamber reached the target temperature, the FTIR background was then taken, followed by introducing the same reaction gas used in the DRM performance test at 12 sccm. The catalyst sample was then allowed to interact with the reaction gas (under continuous flow) while multiple DRIFTS data was taken and recorded under the dark conditions over the next 10 min. It normally takes ~ 3 min before the catalyst surface gets saturated with the reaction gas. Therefore, 10 min is adequate for the catalyst to reach the adsorption equilibrium. After the dark equilibrium DRIFTS spectra were taken, concentrated sunlight was then applied to the sample through the quartz window. The same solar lamp used in the DRM performance test was applied as the light source, the power of the lamp was set at 1200 W. An optical fiber was used to direct the light into the DRIFTS reaction chamber. The intensity of the light exiting the optical fiber was measured to be close to 1 sun, and the light spectrum is shown in Figure S4. Immediately after the concentrated sunlight was applied to the DRIFTS cell, another set of DRIFTS data acquisition was conducted. Multiple DRIFTS data were taken and recorded over the next 5 minutes, which is adequate for the catalyst to reach a new absorption equilibrium under solar irradiation (normally takes less than 1 min). Similar *in situ* DRIFTS analyses were also performed with a CO_2 : Ar = 10 : 90 gas mixture and a CH_4 : Ar = 10 : 90 gas mixture.

3. Results and discussion

3.1 Crystal structure

The XRD patterns of Pt-Ce, Pt-Al-Ce, and Pt-Al are displayed in Figure 1. The characteristic XRD pattern of CeO_2 was found on both Pt-Ce and Pt-Al-Ce, while the characteristic peaks of Pt were not found in the XRD patterns of either sample. The Pt nanoparticles are likely tiny and well distributed on the surface of Pt-Ce and Pt-Al-Ce. By comparing the XRD patterns of Pt-Ce and Pt-Al-Ce, it was noted that the XRD peaks of Pt-Al-Ce are broadened. This observation is likely related to the decreased CeO_2 crystalline size due to the combination of CeO_2 and Al_2O_3. The XRD pattern of Pt-Al indicates that the phase of the Al_2O_3 support as γ-Al_2O_3, elementary Pt [111] peak was found at $2\theta = \sim 39.7^0$, which confirms the existence of Pt in Pt-Al catalyst. Since the weight percentage of Pt is the same in all of the three catalysts, the observation of Pt [111] in Pt-Al suggests that the size of Pt nanoparticles is significantly larger than that on Pt-Ce and Pt-Al-Ce.

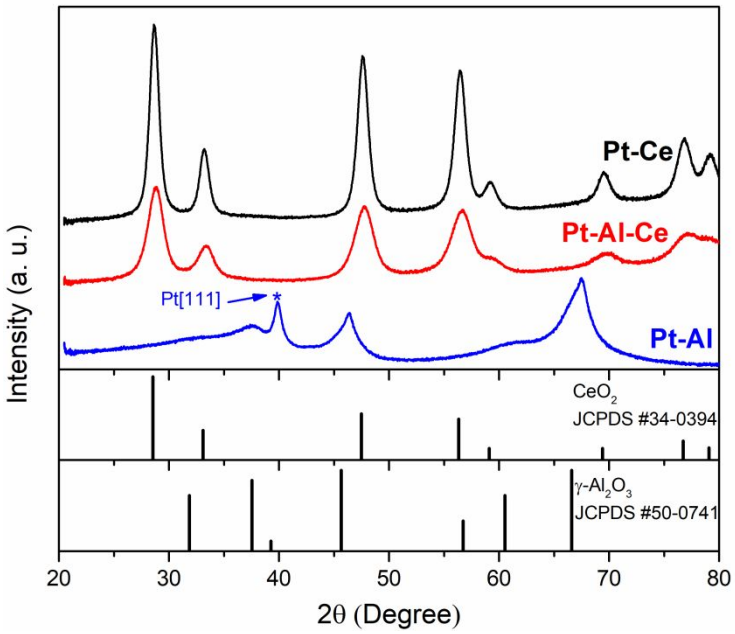

Figure 1. XRD patterns of Pt-Ce, Pt-Al and Pt-Al-Ce.

Interestingly, no characteristic peaks of γ-Al_2O_3 were found in the XRD pattern of Pt-Al-Ce, similar results were also previously observed in several studies in Al_2O_3-CeO_2 hybrid metal oxide materials.[43-45] This is likely related to the low crystallinity of the γ-Al_2O_3 substrate, as evidenced by the wide and less-defined peaks in the XRD pattern of Pt-Al. Since the CeO_2 phase in Pt-Ce shows sharp and well-defined peaks, it is likely that in Pt-Al-Ce, the highly crystallized CeO_2 peaks overshadow those of γ-Al_2O_3, resulting in the absence of γ-Al_2O_3 peaks.

3.2 Morphology

Figure 2 shows the TEM images of Pt-Ce, Pt-Al-Ce, and Pt-Al. As shown in Figure 2a, the particle size of Pt decorated CeO_2 catalyst is ~20 nm, and the catalyst particles show sharp edges and corners. Pt-Al-Ce material particles show a diameter of ~15 nm (Figure 2c) and the particles are oval-shaped. Different from Pt-Ce and Pt-Al-Ce, the particle size of Pt-Al is significantly larger. As shown in Figure 2e, the particle size distribution of Pt-Al ranges from ~100 nm to several hundred nanometers. CeO_2 [111] (0.31 nm) and CeO_2 [100] (0.27 nm) were noted in Pt-Ce and Pt-Al-Ce, according to Figures 2b and d, which coincide with the XRD results. As shown in the CeO_2 lattice Figure 2b, the CeO_2 phase in Pt-Ce material shows long-range order, while the CeO_2 phase in Pt-Al-Ce only exhibits short-range order (Figure 2d). It seems that Al_2O_3 phase breaks down the long-range order of the CeO_2 crystalline in Pt-Al-Ce, which verifies that the phases of Al_2O_3 and CeO_2 are in segregated phases instead of solid solution form. Pt [111] (0.21 nm) spacing was found in Pt-Ce, Pt-Al-Ce, and Pt-Al, confirming the existence of Pt. The sizes of Pt nanoparticles on Pt-Ce, Pt-Al-Ce, and Pt-Al were measured with ImageJ based on a number of TEM images. The average Pt particle size on Pt-Ce, Pt-Al-Ce, and Pt-Al was calculated as 1.9 nm, 1.4 nm, and 6.8 nm, respectively. The histograms of Pt nanoparticle sizes on the three catalysts are included as Figure S5. The Pt nanoparticle sizes on Pt-Al are significantly greater than those on Pt-Ce and Pt-Al-Ce. The large size of Pt nanoparticle size coincides with the XRD pattern of Pt-Al, where Pt [111] peak

is prominent.

To confirm the existence of the Al element in Pt-Al-Ce, elemental mapping was performed by energy-dispersive X-ray spectroscopy (EDS). The EDS result is included in the Supporting Information as Figure S6. The elemental mapping of Pt-Al-Ce shows strong signals of Ce and Al, confirming Ce and Al are major elements in Pt-Al-Ce. Pt was also found in the EDS mapping, while Pt signal is much weaker compared to those of Ce and Al, which is reasonable due to the low concentration of Pt (1.0 wt.%) in Pt-Al-Ce.

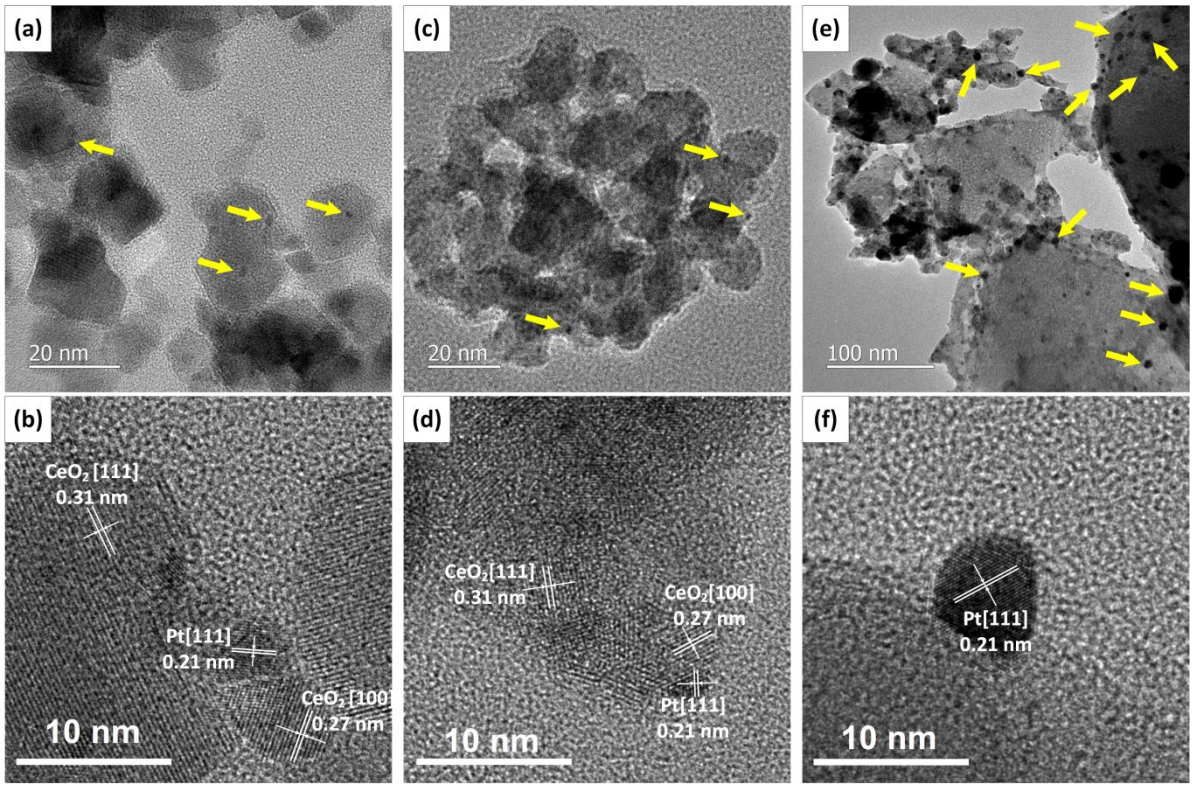

Figure 2. TEM images of Pt-Ce (a & b), Pt-Al-Ce (c & d), and Pt-Al (e & f); yellow arrows point to Pt nanoparticles.

3.3 Surface chemical properties

X-ray photoelectron spectroscopy (XPS) analysis on Ce *3d* orbital was conducted on Pt-Ce and

Pt-Al-Ce to investigate the effect of Al_2O_3-CeO_2 incorporation on the chemical states of CeO_2. Prior to the XPS testing, the catalysts were pre-reduced in Ar/H_2 gas mixture as they would be in DRM performance tests. XPS analyses on Pt or Al were not performed as the XPS binding energies of the two elements overlap, making it impractical to reach meaningful results or conclusions. The existence of Ce^{3+} in the catalyst surface indicates the formation of oxygen vacancies, likely generated during the H_2 reduction process. The oxygen vacancy has been deemed as a key factor for achieving high DRM performance.[15, 46] As shown in Figure 3, the Ce *3d* spectra can be well deconvoluted into Ce^{4+} and Ce^{3+}, where v_o, v', u_o, and u' correspond to Ce^{3+}; v, v'', v''', u, u'', and u''' correspond to Ce^{4+}.[15, 47-49] Based on the Ce *3d* deconvolution results, the molar ratios of $Ce^{3+}/(Ce^{3+} + Ce^{4+})$ on Pt-Ce and Pt-Al-Ce are calculated to be 24.3% and 24.7%, respectively. It seems that the incorporation of Al_2O_3 into Pt-CeO_2 does not significantly promote the formation of Ce^{3+}. The $Ce^{3+}/(Ce^{3+} + Ce^{4+})$ value on both of the catalysts are similar; however, if considering the high concentration of the Al_2O_3 incorporation in Pt-Al-Ce, the oxygen vacancy concentration on Pt-Al-Ce can be significantly lower than that on Pt-Ce.

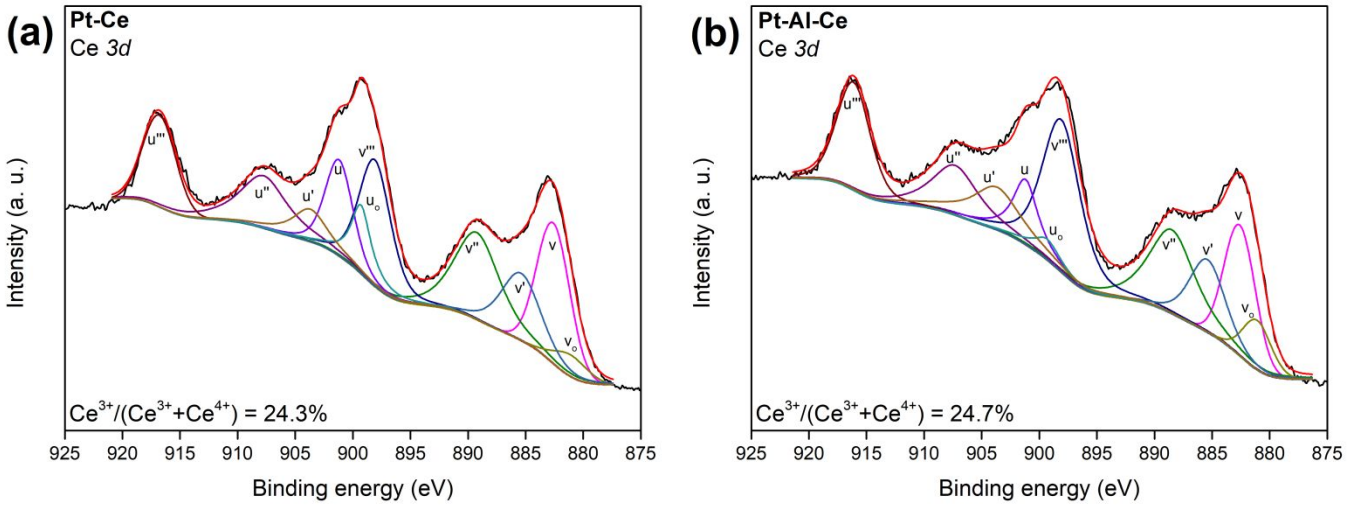

Figure 3. Deconvolution of Ce *3d* XPS spectra on Pt-Ce and Pt-Al-Ce catalysts.

To better compare the surface oxygen vacancies concentrations between Pt-Ce and Pt-Al-Ce, the deconvolution of O *1s* was also performed. The difference in binding energy values of the lattice oxygen (O_L) on Al_2O_3 and CeO_2 was found to be very close to each other.[50-53] Therefore, the two types of lattice oxygen atoms were considered as a whole, whose peak is located at ~ 529.9 eV. The peak at ~532.0 eV was identified as adsorbed oxygen (O_A) on oxygen vacancies, which can be applied to determine the concentration of surface vacancies.[50, 51, 54] Based on the O *1s* deconvolution result shown in Figure 4, the O_A concentrations on Pt-Ce and Pt-Al-Ce were calculated as 27.0% and 15.5%, respectively. Compared with Pt-Ce, Pt-Al-Ce exhibits a relatively lower concentration of oxygen vacancies, which is reasonable as only CeO_2 is capable to produce oxygen vacancies in a reducing environment and CeO_2 is diluted due to the existence of Al_2O_3 in Pt-Al-Ce.

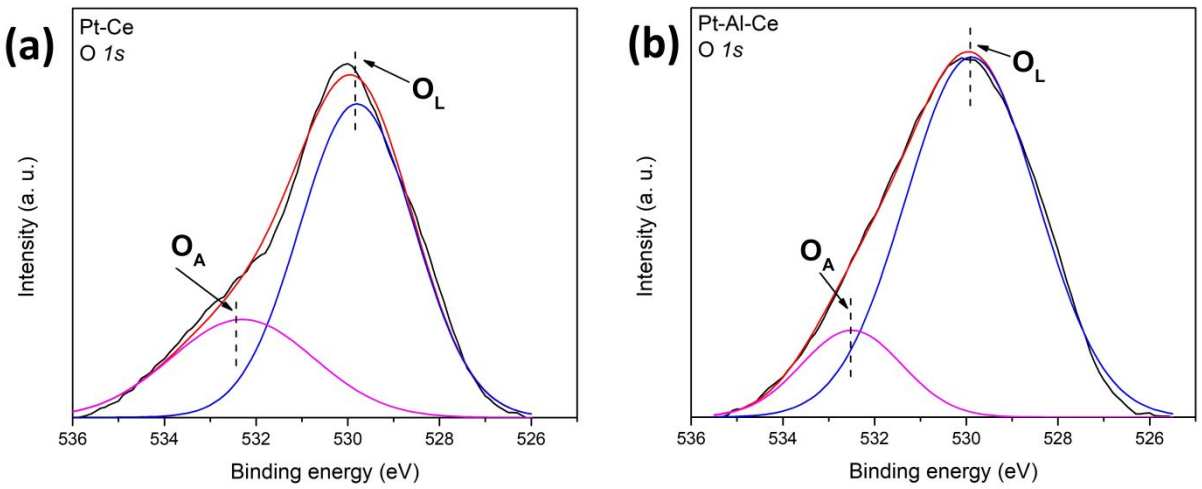

Figure 4. Deconvolution of O *1s* XPS spectra on Pt-Ce and Pt-Al-Ce catalysts.

3.4 Optical properties

To investigate the optical properties and calculate the bandgaps of the as-prepared catalysts, UV-Vis diffuse reflectance spectra and bandgap analyses were performed. As shown in Figure 5a, Pt-Ce absorbs light mainly in the wavelength range below 400 nm, showing two major absorption bands located

at 250 nm and 351 nm, in agreement with the CeO_2 light absorption property reported in a previous study.[55] Pt-Al-Ce also shows a major light absorption to photons with a shorter wavelength than 400 nm, while the absorption band at ~250 nm shows a slight intensity decline. Different from Pt-Ce and Pt-Al-Ce, Pt-Al only shows absorption at ~258 nm, which is identified as the light absorption of alumina.[56] The light absorption of Pt nanoparticles likely causes the light absorption in the visible light range.

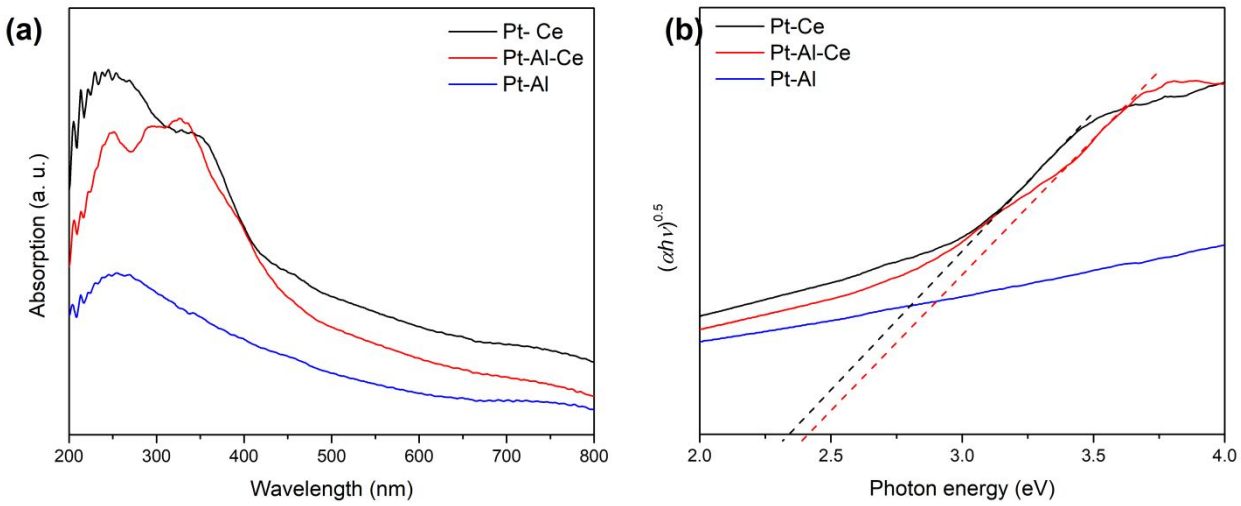

Figure 5. UV-Vis light absorption spectra (a) and Tauc plots (b) of Pt-Ce, Pt-Al-Ce, and Pt-Al materials.

Bandgap analysis was performed with Tauc plot based on the procedure reported by Makula *et al*. previously.[57] Figure 5b shows the bandgap analyses for Pt-Ce, Pt-Al-Ce, and Pt-Al. The bandgaps of Pt-Ce and Pt-Al-Ce were calculated as 2.3 eV and 2.4 eV, respectively. Pt-Al-Ce material only shows a bandgap value change of 0.1 eV; it seems that the existence Al_2O_3 does not cause a significant bandgap variation on CeO_2 component in Pt-Al-Ce. However, according to the Tauc plot of Pt-Al, it is not plausible to determine the bandgap value of Pt-Al. This result suggests Pt-Al catalyst is not photoactive. The obtained bandgap value of Pt-Ce is lower compared with the calculated values in our previous reported values.[14, 15] As mentioned, the catalysts were reduced prior to the UV-Vis diffuse reflectance

measurements. The oxygen vacancy generated from the reduction process is likely responsible for the narrowed bandgaps of Pt-Ce and Pt-Al-Ce.[58, 59]

3.5 DRM performance

DRM performance data of Pt-Al-Ce, Pt-Ce, and Pt-Al at 700 ℃ under both dark conditions and concentrated sunlight were presented in Figure 6. The three catalysts show structure and morphology stability after the experiments, as shown in Figures S7 and S8. The numerical results of the DRM performance are listed in Table 1, where the listed values are the averages of all DRM performance data presented in Figure 6. Both Pt-Ce and Pt-Al-Ce showed good stability under both dark and light conditions for the DRM process at 700 ℃. Both catalysts showed DRM performance enhancement under light conditions compared with those in dark conditions, as shown in Figure 6. Notably, under concentrated solar irradiation, Pt-Al-Ce delivered a near-unity H_2/CO production ratio of 0.99, which is significantly improved compared with that of Pt-Ce (0.77 under light conditions).

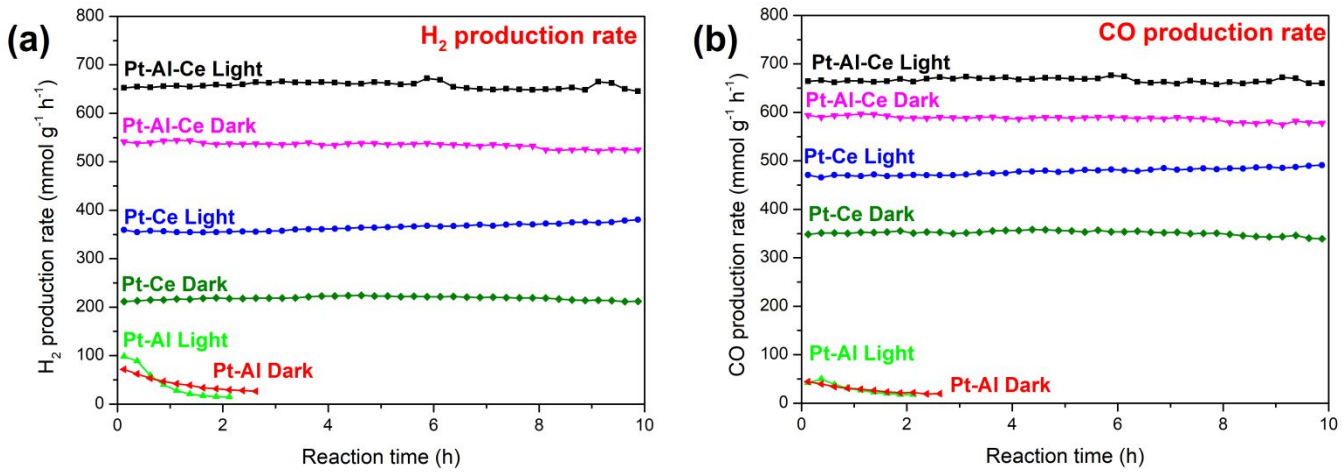

Figure 6. DRM performance: (a) H_2 production and (b) CO production of Pt-Ce, Pt-Al and Pt-Al-Ce at 700 ℃ under light and dark conditions.

Table 1. DRM performance of Pt-Ce, Pt-Al-Ce and Pt-Al at 700 ℃ (average of data in Figure 6).

Sample ID	H_2 production rate ($mmol \cdot g^{-1} \cdot h^{-1}$)	CO production rate ($mmol \cdot g^{-1} \cdot h^{-1}$)	H_2/CO ratio
Under dark conditions			
Pt-Ce	218	351	0.62
Pt-Al-Ce	535	588	0.91
Pt-Al	42	28	1.50
Under solar irradiation			
Pt-Ce	365	477	0.77
Pt-Al-Ce	657	666	0.99
Pt-Al	43	30	1.44

Contrastingly, Pt-Al deactivates fast under both reaction conditions within less than 2 h in the DRM process. No significant difference in DRM performance was observed related to solar irradiation. Al_2O_3 is not considered photoactive. It is, therefore, reasonable that the concentrated sunlight does not make a significant difference in the DRM performance of the Pt-Al catalyst. Regarding the DRM catalyzing stability of Pt-Al, as previously reported by Hambali *et al.*,[32] a DRM catalyst with an over-acidic surface may result in deactivation in the DRM process to coke accumulation. Although Al_2O_3 is a type of material showing only weak surface acidity under DRM reaction conditions,[33] it seems that the surface acidity of pure Al_2O_3 support is already too high for the DRM process to maintain a stable catalytic activity. As shown in Table 1, the H_2/CO ratios on Pt-Al under light and dark conditions were calculated to be 1.50 and 1.44, respectively. A value of H_2/CO ratio higher than 1.0 in the DRM process suggests a faster methane dissociation rate than coke carbon gasification rate, which leads to coke accumulation and causes performance deactivation.

As determined by the TEM analyses, there is a difference between the size of Pt nanoparticles on Pt-Ce (1.9 nm) and Pt-Al-Ce (1.4 nm). The size of Pt nanoparticles deposited on the catalysts is a crucial factor in determining the DRM reaction rate. However, little information was found in the literature on

the Pt nanoparticle sizes on the reaction rate of DRM reactions. In a similar materials system, however, Gascon *et al*.[60] investigated the role of Rhodium (Rh) particle size on DRM reaction rates, where the Rh nanoparticles were deposited on three substrates, namely CeO_2, CeO_2-ZrO_2, and ZrO_2. It was found that the DRM reaction rates on the catalysts showed a linear correlation with the Rh nanoparticle size in the range of 1.6 - 8.0 nm. This study applied a similar catalyst system and conducted the same reaction process as in the present work. More importantly, as a type of noble metal, Rh nanoparticles promote the DRM reaction rate in a similar way as Pt does. Based on the work of Gascon *et al*., given the fact that Rh is generally more active as an active species than Pt in the DRM process,[61] the small difference in Pt nanoparticle sizes between Pt-Ce and Pt-Al-Ce is unlikely to make a significant difference in the DRM reaction rates on Pt-Ce and Pt-Al-Ce.

An apparent synergy effect of Al_2O_3 and CeO_2 as catalyst support is observed on Pt-Al-Ce. Pt-Al-Ce considerably outperforms both Pt-Ce and Pt-Al in H_2 and CO production rate. Compared with Pt-Ce, Pt-Al-Ce shows significant enhancement in CO and H_2 production rate under both light and dark conditions (67.2% and 144.8% enhancements in CO and H_2 under dark, respectively; 39.6% and 80.0% improvements in CO and H_2 under light, respectively). Compared with Pt-Al, Pt Al-Ce exhibits good stability, in addition to the notably promoted H_2 and CO production rates. The significant improvement in H_2 generation rate on Pt-Al-Ce suggests that methane dissociation was strongly promoted. In this sense, the incorporation of Al_2O_3 with CeO_2 is advantageous due to the high efficiency of CeO_2 in the oxidation of surface deposited coke into CO.[27, 62, 63] In this regard, in Pt-Al-Ce material, Al_2O_3-CeO_2 support is likely bi-functional: firstly, Al_2O_3 promotes methane dissociation on Pt nanoparticles, resulting in improved H_2 generation; secondly, CeO_2 acts as catalyst performance stabilizer by eliminating any possible coke formed from methane dissociation. It is likely that the two possible mechanisms work jointly to promote the DRM performance on Pt-Al-Ce catalyst.

To confirm the above hypotheses and further investigate the synergy effect of Al_2O_3 and CeO_2 in the Al_2O_3-CeO_2 binary substrate, a CeO_2-rich Pt-Al-Ce catalyst (Al : Ce molar ratio = 2 : 10, noted as Ce-Rich-PAC) and an Al_2O_3-rich Pt-Al-Ce catalyst (Al : Ce molar ratio = 10 : 2, noted as Al-Rich-PAC) were prepared and tested for DRM performance under solar irradiation at 700 ℃, and the results are shown in Figure S9. Ce-Rich-PAC shows stable catalytic activities, and the 10-h average of CO and H_2 production rates of Ce-Rich-PAC are 602 $mmol \cdot g^{-1} \cdot h^{-1}$ and 549 $mmol \cdot g^{-1} \cdot h^{-1}$, respectively. Even with a low Al_2O_3 incorporation concentration in the catalyst, Ce-Rich-PAC shows notable enhancements in catalytic performance than those of Pt-Ce. The H_2/CO production ratio of Ce-Rich-PAC was 0.91, considerably higher than that of Pt-Ce and only slightly lower than that of Pt-Al-Ce. In contrast to the stable DRM performance of Ce-Rich-PAC, Al-Rich-PAC shows a deteriorating catalytic performance over time: the initial CO and H_2 production rates are 641 $mmol \cdot g^{-1} \cdot h^{-1}$ and 728 $mmol \cdot g^{-1} \cdot h^{-1}$, respectively, which dropped to 581 $mmol \cdot g^{-1} \cdot h^{-1}$ and 596 $mmol \cdot g^{-1} \cdot h^{-1}$ after 10 h, respectively. Interestingly, the initial CO production rate on Al-Rich-PAC is slightly lower than that of Pt-Al-Ce, but the initial H_2 production rate on Al-Rich-PAC is ~9% higher than that of Pt-Al-Ce. This result again implies that Al_2O_3 promotes H_2 generation from methane dissociation. Over the 10 h test, the H_2/CO production ratio on Al-Rich-PAC is always greater than 1.0, suggesting a faster methane dissociation reaction rate and coke accumulation on the catalysts, which leads to deactivation in DRM performance. Despite the DRM catalytic deactivation of Al-Rich-PAC over time, compared with Pt-Al, Al-Rich-PAC exhibits remarkable improvements in both catalytic performance and stability, even with a low CeO_2 incorporation concentration. The enhancements are likely related to the superior coke gasification ability of CeO_2, which minimizes coke accumulation and preserves the activity of the catalyst.[64] However, with a low CeO_2 incorporation amount, Al-Rich-PAC still shows deterioration in catalytic performance over time.

To determine the effect of Pt concentration of Pt-Al-Ce catalyst on the DRM process, varied

amount of Pt (0.25 wt.%, 0.5 wt.%, and 2 wt.%) was loaded on the equimolar Al_2O_3-CeO_2 hybrid substrate (denoted as 0.25-Pt-Al-Ce, 0.5-Pt-Al-Ce, and 2-Pt-Al-Ce, respectively) and applied for the DRM process. All of the catalysts showed a stable DRM catalyzing performance, the averaged DRM performances were listed and compared in Table 2. It is clear that a higher Pt loading concentration is favorable in promoting the H_2 and CO production rate as well as the H_2/CO ratio. However, by comparing Pt-Al-Ce with 2-Pt-Al-Ce, especially those under solar irradiation, the increase in the H_2/CO ratio is marginal when Pt loading is over 1.0 wt.%, despite the slight enhancement in H_2 and CO production. Since Pt is a noble metal and expensive, by taking the cost of Pt into consideration, it is safe to reach the conclusion that 1.0 wt.% of Pt loading is optimal.

Table 2. DRM catalytic performance of Pt-Al-Ce catalyst with varied Pt loading amount.

Sample ID	H_2 production rate ($mmol \cdot g^{-1} \cdot h^{-1}$)	CO production rate ($mmol \cdot g^{-1} \cdot h^{-1}$)	H_2/CO ratio
Under dark conditions			
0.25-Pt-Al-Ce	225	337	0.67
0.5-Pt-Al-Ce	446	528	0.85
Pt-Al-Ce	535	588	0.91
2-Pt-Al-Ce	682	685	0.99
Under solar irradiation			
0.25-Pt-Al-Ce	313	424	0.74
0.5-Pt-Al-Ce	489	554	0.88
Pt-Al-Ce	657	666	0.99
2-Pt-Al-Ce	729	717	1.02

To further investigate the role of solar irradiation in the DRM process on Pt-Al-Ce catalyst, DRM performance tests at 650 ℃ and 600 ℃ under both dark and light conditions were conducted on Pt-Al-Ce catalyst, the performance results of the test are listed along with the 700 ℃ data in Table S1. The ln(r) – 1000/T correlations were plotted in Figure 7 according to the Arrhenius equation based on the data listed

in Table S1. The ln(r) - 1000/T regression plots show a good linear correlation, and the linear regressions of the four datasets returned R^2 values close to 1.0, indicating accurate regression results. The apparent activation energy values were listed in Table 3 based on the calculated slopes of each regression curve.

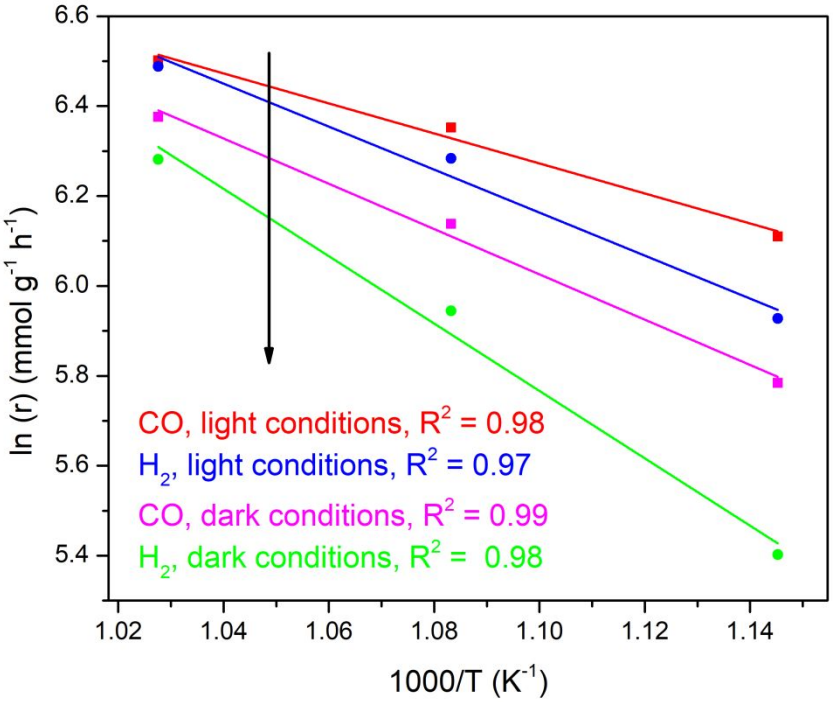

Figure 7. Arrhenius ln (r) - 1000/T plot for H_2 and CO gas production rate in DRM process on Pt-Al-Ce catalyst under both dark and light conditions.

Table 3. The apparent activation energy of H_2 and CO production on Pt-Al-Ce under dark and light conditions.

Gas species	Apparent E_a (kJ/mol)	
	Dark	Light
H_2	62.3	39.8
CO	41.9	27.8

As shown in Table 3, the apparent activation energy for H_2 and CO production under dark

conditions is 62.3 kJ/mol and 41.9 kJ/mol, respectively. The apparent E_a of H_2 and CO production under solar irradiation are 39.8 kJ/mol and 27.8 kJ/mol, which is significantly lowered compared with those calculated under dark conditions, similar observations on the reactant activation effect of light irradiation in DRM process has also been documented by Yoshida *et al.*[65] and Miyauchi *et al.*[66-68] It seems that the sunlight assisted in the activation of the reactants in the DRM process on Pt-Al-Ce catalysts. However, according to Figure 6 and Table 1, H_2 and CO production efficiency on Pt-Al is insensitive to light irradiation. Therefore, irradiation alone does not directly activate the reactants. Photoactive CeO_2 seems to be the media assisting the conversion of photon energy into chemical energy and facilitating the reaction. To determine the photoactivities of CeO_2 in Pt-Ce and Pt-Al-Ce, XPS deconvolution of Ce *3d* of spent Pt-Ce and Pt-Al-Ce under both light and dark conditions under 700 ℃ was performed, the results are shown in Figure S10. The light excitation can weaken the Ce-O bonds in CeO_2 and lead to the generation of Ce^{3+} and oxygen vacancies ($Ce^{4+} + h\nu \rightarrow Ce^{3+} + V_O$).[15, 69] After DRM reaction under the dark conditions, both Pt-Ce and Pt-Al-Ce exhibit lower molar ratios of $Ce^{3+}/(Ce^{3+} + Ce^{4+})$, valued at 17.4% and 15.6%, respectively, compared with fresh catalysts (fresh Pt-Ce: 24.3%, fresh Pt-Al-Ce: 24.7%) in Figure 3, which is likely due to the oxidation of Ce^{3+} to Ce^{4+} by CO_2 in the DRM process.[15, 69] Contrastingly, significantly higher molar ratios of $Ce^{3+}/(Ce^{3+} + Ce^{4+})$ on both catalysts was observed after the DRM reaction under the irradiation of the concentrated sunlight (Pt-Ce: 39.1%, Pt-Al-Ce: 49.8%). This result suggests that the photoactive CeO_2 component in Pt-Ce and Pt-Al-Ce could contribute to the DRM performance under light irradiation through photocatalysis.

To further verify the role of photocatalysis in the photo-driven DRM process on Pt-Al-Ce catalyst, a control experiment was conducted at 700 ℃ with a 530-nm long-pass filters. The cut-off photon energy of the 530-nm filter is 2.34 eV, which is slightly lower than the bandgap energy of Pt-Al-Ce (2.4 eV). Table 4 shows the comparison of 10-h average Pt-Al-Ce DRM performance under full-spectrum, 530 nm

cut-off, and dark conditions. Under 530 nm cut-off condition, where the photon energy is lower than the bandgap energy of Pt-Al-Ce, the DRM performance is almost the same as that under dark conditions. This result suggests that light irradiation enhances the DRM reaction through photocatalytic excitation of the catalyst, where photon energy is converted to chemical energy conversion and leads to the significantly lower apparent activation energy for the production of H_2 and CO.

Table 4. DRM catalytic performance of Pt-Al-Ce at varied light irradiation conditions at 700 ℃.

Reaction conditions	H_2 production rate ($mmol \cdot g^{-1} \cdot h^{-1}$)	CO production rate ($mmol \cdot g^{-1} \cdot h^{-1}$)
Full spectrum	657	666
>530 nm cut-off	531	593
Dark	535	588

3.6 *In situ* DRIFTS analysis

To understand the effect of solar irradiation and investigate the intermediates involved in the photo-thermal driven DRM process, *in situ* DRIFTS analysis was conducted at various temperatures on Pt-Ce, Pt-Al-Ce, and Pt-Al under dark and light conditions in three gas environments: (1) DRM reaction gas (CO_2, and CH_4), (2) CO_2 only, and (3) CH_4 only.

As shown in Figure 8, the exposure of DRM reaction gas to Pt-Ce and Pt-Al-Ce led to the generation of surface intermediates including formate (HCOO-),[70-72] bidentate carbonate (b-CO_3^{2-}),[72-75] and monodentate carbonate (m-CO_3^{2-}).[76, 77] The peaks located at 1338 cm^{-1} and 1308 cm^{-1} were identified as gaseous CH_4[78] in the reactions. The doublet bands found at 2069 cm^{-1} and 1971 cm^{-1} were identified as CO molecules linearly bonded on Pt atoms (Pt-CO).[79-82] The CO molecules were likely originated from CO_2 reduction taking place on the catalyst surface. The absorption band located at 2069 cm^{-1} indicated the existence of linearly adsorbed CO on Pt, while the shoulder band centered at ~1971 cm^{-1} indicated the

coverage of CO molecules on the boundary of Pt and the metal oxide support.[79-82] On Pt-Al, only Pt-CO and bicarbonate bands[83, 84] were observed. Gaseous CO production was also observed as the duplet band at 2178 cm^{-1} and 2109 cm^{-1} at a temperature higher than 400 ℃ on Pt-Al.

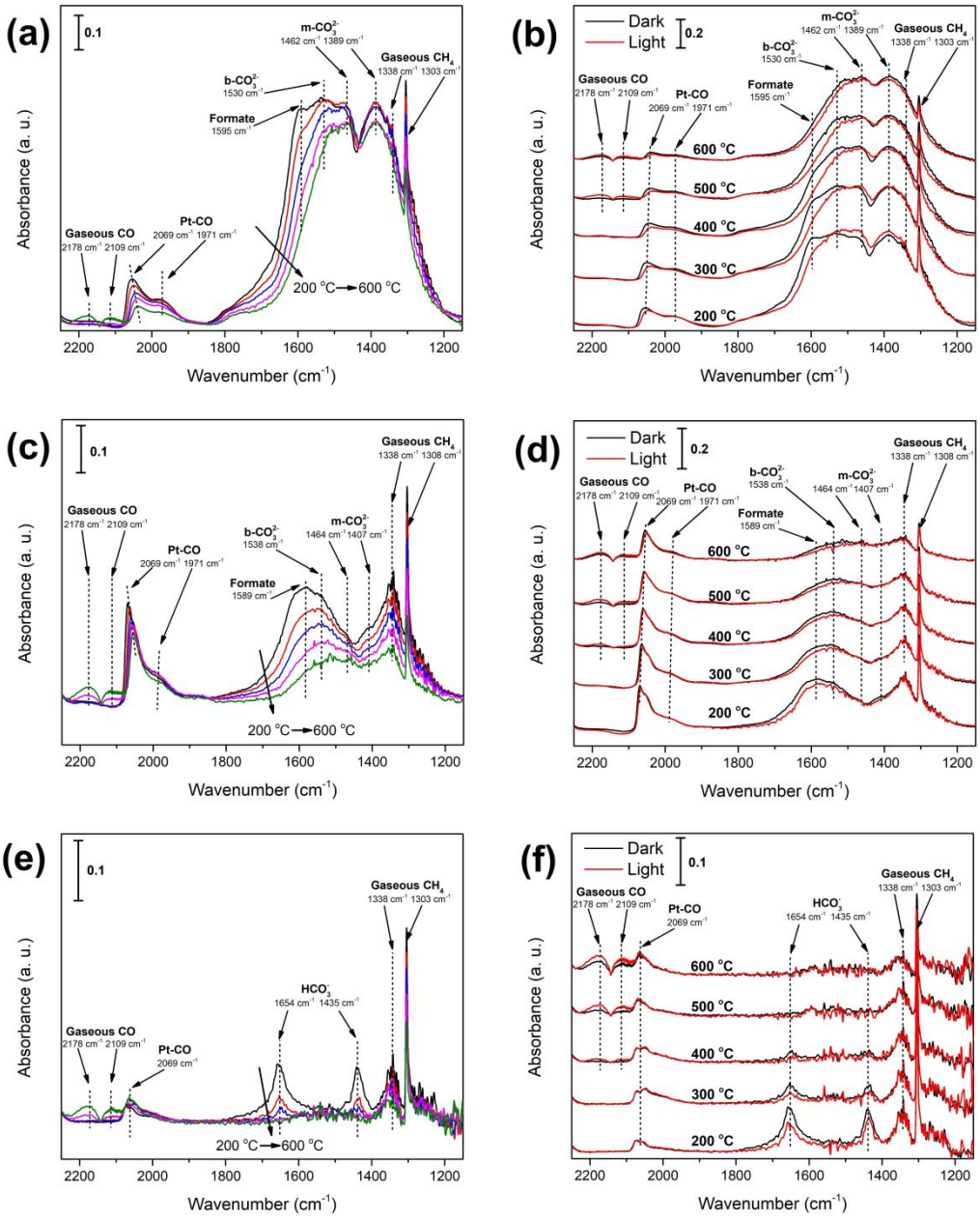

Figure 8. *In situ* DRIFTS spectra at DRM reaction conditions in the dark on (a) Pt-Ce, (c) Pt-Al-Ce, (e) Pt-Al, and dark-light comparison on (b) Pt-Ce, (d) Pt-Al-Ce, (f) Pt-Al.

Figure 8a shows the surface intermediates behavior on Pt-Ce under reaction gas atmosphere to temperature increase under dark conditions. All surface intermediates were found to show a decrease in absorption intensity due to the temperature increase. It seems that the formate intermediates are quite sensitive to temperature increases: the formate band intensity almost halved after the temperature increased from 200 ℃ to 600 ℃. Only a small intensity diminish was found on m-CO_3^{2-} and b-CO_3^{2-}. A red-shifting effect was observed on the Pt-CO band as temperature increases, which was likely due to the declined CO adsorption reducing the repulsion forces among CO molecules and leading to red shifting of the CO absorption band,[85] indicating CO desorption.

Figure 8b shows the comparison between light and dark *in situ* DRIFTS results obtained on Pt-Ce. Under light irradiation, almost all of the surface intermediates showed a slight intensity decline. To rule out the thermal effect of the light irradiation, an IR thermometer was used to determine the temperature change of the sample in the *in situ* DRIFTS cell upon the light irradiation at room temperature. After ~5 min of sunlight irradiation, only a temperature rise of ~5 ℃ was observed on the catalyst surface. With such a minor temperature change at room temperature, the temperature change caused by the light irradiation may be negligible for tests conducted at 200 - 600 ℃. The most noticeable change in the spectra is the sharp intensity decline of the formate band at ~1595 cm^{-1} under light irradiation. The intensity of b-CO_3^{2-} was also found to decline under light irradiation. It seemed that m-CO_3^{2-} was relatively stable upon the light irradiation. Both formate and b-CO_3^{2-} have been viewed as important surface intermediates in CO generation in the DRM process. The intensity declines in the two surface intermediates suggest an accelerated rate of the surface intermediates participating in the reaction process.[86] The activation energy calculation chart shows that solar irradiation activates the surface intermediates and promotes the DRM reactions.

Similar surface intermediates were found on Pt-Al-Ce in dark conditions under reaction gas

atmosphere, as shown in Figure 8c. Compared with Pt-Ce, the intensities of all of the carbonate absorption bands in the range of 1600 - 1200 cm^{-1} were significantly weaker on Pt-Al-Ce, which was likely due to the lower concentration of CeO_2 in Pt-Al-Ce material. Interestingly, the Pt-CO absorption band on Pt-Al-Ce was considerably stronger than that on Pt-Ce. In addition, the Pt-CO band on Pt-Al-Ce seemed to be less sensitive to temperature increase: only a small drop in Pt-CO peak height was recorded while the temperature increased from 200 ℃ to 600 ℃. The results indicate (1) a higher number of Pt nanoparticle active reaction sites, and (2) more reactive Pt nanoparticles on Pt-Al-Ce than those on Pt-Ce, which is likely promoted by the synergy effects between Al_2O_3 and CeO_2 in Pt-Al-Ce material. Similar to Pt-Ce, as temperature rises, the intensity of absorption bands on Pt-Al-Ce declines. Similar to the observations on Pt-Ce, formate showed the most intensity decrease as temperature increased, b-CO_3^{2-} and m-CO_3^{2-} was also found to be sensitive to temperature increase. Similar to Pt-Ce, upon the concentrated solar irradiation, the formate and b-CO_3^{2-} intermediates showed a slight decrease in absorption band intensity, as shown in Figure 8d, suggesting a promoted reaction rate in the DRM process.

Distinct from Pt-Ce and Pt-Al-Ce, only bicarbonate and Pt-CO were found on the surface of Pt-Al after contacting with the reaction gas. The intensity of Pt-CO absorption band on Pt-Al was significantly weaker compared with Pt-Ce or Pt-Al-Ce, indicating fewer Pt nanoparticle active sites and less reactive Pt nanoparticles. The HCO_3^- intermediates seemed to be very sensitive to temperature increases. By increasing the temperature from 200 ℃ to 400 ℃ under dark conditions, the HCO_3^- absorption intensity decreased fast and disappears at 500 ℃, as shown in Figure 8e. Since DRM tests were conducted at high temperatures in this study, it is likely that bicarbonate is not an active intermediate in the DRM process. The low CO_2 affinity on Al_2O_3 might partially contribute to the poor DRM performance on Pt-Al.

To get a deeper understanding of the surface interaction between the catalysts and CO_2 or CH_4, *in situ* DRIFTS analyses were conducted under CO_2 and CH_4 atmosphere, respectively. The *in situ* DRIFTS

results of Pt-Ce and Pt-Al-Ce obtained under a CO_2 atmosphere were shown in Figure 9. Only weak Pt-CO bands were found on Pt-Al under CO_2 atmosphere, no carbonates bands were found, indicating low CO_2 affinity of Pt-Al catalyst. The spectra obtained with Pt-Al are included in Figure S11. In Figure 9, Pt-Ce and Pt-Al-Ce showed similar surface intermediates and DRIFTS spectra shape when the two catalysts were exposed to CO_2 gas. A formate band was found on both Pt-Ce and Pt-Al-Ce in the 1200-1400 cm^{-1} range (Figures 9a-d),[70] which was overshadowed by CH_4 gas in Figure 8. Both formate bands were sensitive to temperature increase and concentrated solar irradiation, coinciding with the results observed under the DRM gas atmosphere. Similar to the observation made in Figure 8, Pt-Al-Ce shows a stronger Pt-CO band, suggesting highly active and concentrated Pt nanoparticle reactions sites.

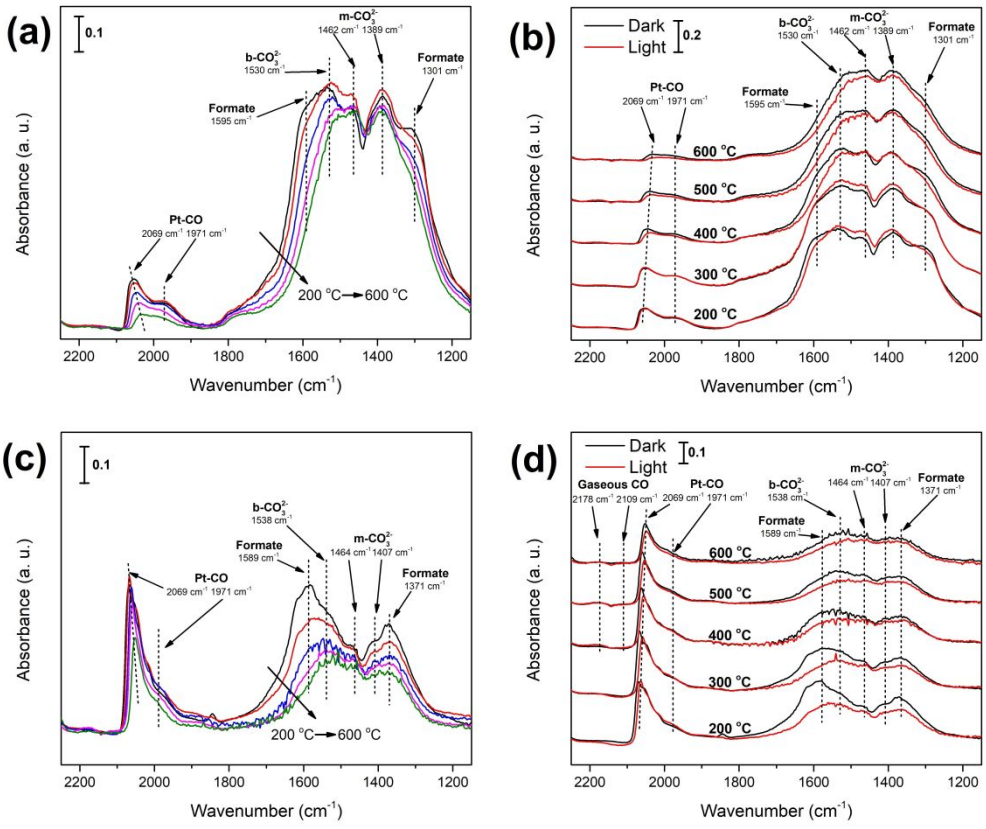

Figure 9. *In situ* DRIFTS spectra under CO_2 atmosphere in the dark on (a) Pt-Ce, (c) Pt-Al-Ce, and dark-light comparison on (b) Pt-Ce, (d) Pt-Al-Ce.

Under light irradiation, Pt-Ce shows formate absorption band intensity decline at all temperatures. Under 200 ℃ and 300 ℃, interestingly, it was found that the concentrated solar irradiation led to increases m-CO_3^{2-} and b-CO_3^{2-} band intensity on Pt-Ce. The light irradiation likely caused oxygen vacancy generation on CeO_2 through a photocatalytic self-reduction process ($CeO_2 + h\nu \rightarrow CeO_{2-x} + O_2$),[87] which further promoted CO_2 adsorption and led to a slight intensity increase in m-CO_3^{2-} and b-CO_3^{2-} bands. At higher temperatures, all band intensities of surface absorbed intermediates drop under light irradiation. Formate, m-CO_3^{2-}, and b-CO_3^{2-} are active intermediates in CO_2 reduction reactions.[86, 88] The photo-induced band intensity declines likely suggest the occurrence of CO_2 reduction. However, gaseous CO bands were not observed in Figure 9b, which is possibly due to the very low gaseous CO concentration on Pt-Ce. As shown in Figure 9d, the light irradiation on Pt-Al-Ce resulted in considerable band intensity drops for the formate, m-CO_3^{2-}, and b-CO_3^{2-} in the temperature range of 200 ℃ - 500 ℃. A weak gaseous CO band was observed starting at 500 ℃, confirming the occurrence of CO_2 reduction reactions. The existence of a gaseous CO band with Pt-Al-Ce catalyst suggests higher reactivity of Pt-Al-Ce compared to Pt-Ce.

The *in situ* DRIFTS results obtained under the CH_4 atmosphere are shown in Figure 10, where spectra obtained 300 - 600 ℃ were shown. For Pt-Ce, starting from 300 ℃, strong carbonate bands were observed in the range of 1200 - 1600 cm^{-1}. The carbonates are likely the product of CH_4 oxidation by CeO_2. Weak Pt-CO bands were found. Compared with the Pt-CO bands observed under reaction gas and CO_2 atmospheres, a significant redshift was detected: from 2069 cm^{-1} under CO_2-rich atmosphere to 2033 cm^{-1} under CH_4 atmosphere, indicating a low CO coverage on Pt nanoparticles. This observation is reasonable as only a trace amount of CH_4 can be converted into CO on Pt-Ce surface under a CH_4 atmosphere. Formate was not found from the CH_4-DRIFTS results, which suggests that CO_2 is the source for formate intermediate generation. The intensities of the b-CO_3^{2-} bands observed under CH_4 atmosphere

were considerably lower than those found under CO_2 or reaction gas atmosphere. This is likely because the conversion from m-CO_3^{2-} to b-CO_3^{2-} requires excessive CO_2 supply, which, however, was lacking under the CH_4 atmosphere. In addition, it does not seem that the surface intermediates are sensitive to concentrated solar irradiation under the CH_4 atmosphere, as compared by Figure 10a and b. Pt-Al-Ce showed similar behavior as noticed on Pt-Ce catalyst and similar surface intermediates were found (Figures 10c and d). However, compared with Pt-Ce, Pt-Al-Ce showed a significantly stronger Pt-CO absorption band. The Pt-CO band on Pt-Al-Ce was evident even at a low temperature of 300 ℃, which is a clear indicator of the occurrence of strong CH_4 oxidation. This result suggests that the Pt-Al-Ce material shows substantially higher surface reactivity compared to Pt-Ce. The DRIFTS data obtained on Pt-Al is included in Figure S12. No carbonate intermediates were found on Pt-Al, suggesting poor catalyst-CH_4 surface interaction. Surprisingly, however, a weak Pt-CO peak was found on Pt-Al under the CH_4 atmosphere. Without the presence of CO_2, the origin of Pt-CO can only be the oxidation of CH_4. It seems that Pt-Al is capable of dissociating trace amounts of CH_4 even at 300 ℃. By combining the fact that Pt-CO was found on Pt-Al-Ce and Pt-Al under CH_4 atmosphere, it seems the existence of Al_2O_3 promotes the dissociation of CH_4, even at a relatively low temperature.

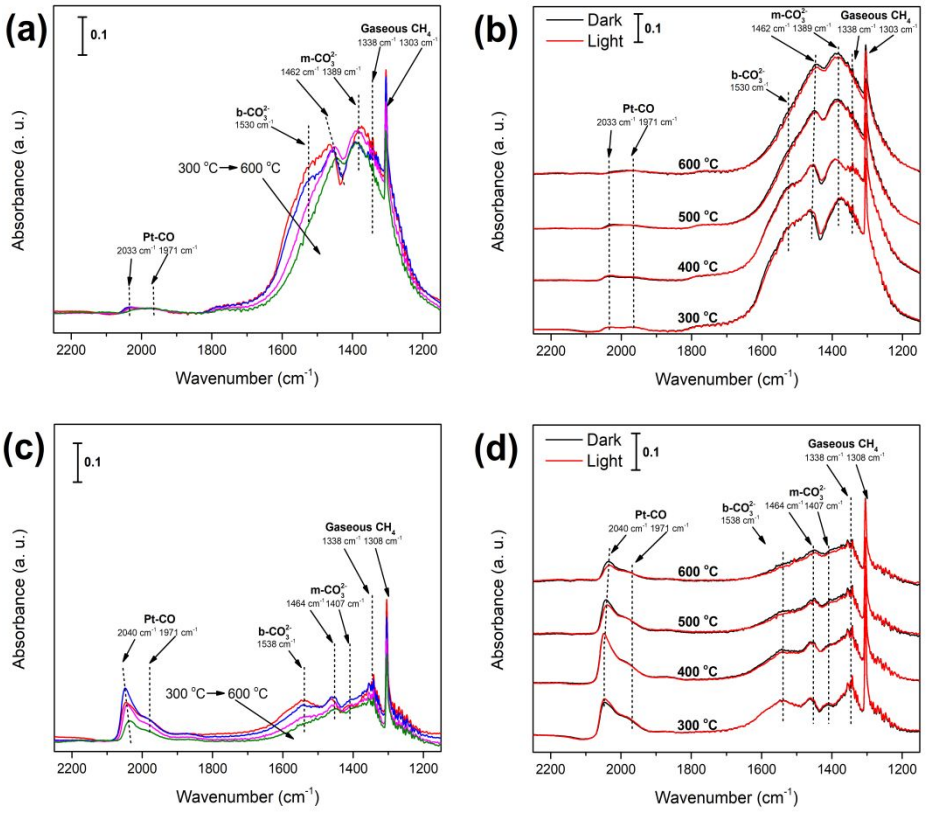

Figure 10. *In situ* DRIFTS spectra under CH_4 atmosphere in the dark on (a) Pt-Ce, (c) Pt-Al-Ce, and dark-light comparison on (b) Pt-Ce, (d) Pt-Al-Ce.

The observation that Pt nanoparticles on Pt-Al-Ce were more reactive and provides more reaction sites is well aligned with material characterizations and the DRM catalytic performances. Firstly, the synergy effects between Al_2O_3 and CeO_2 significantly promote the reactivity of Pt nanoparticles on Pt-Al-Ce. Secondly, since methane dissociation in the DRM process takes place on Pt nanoparticles,[69] a higher reactivity in Pt nanoparticles suggests a promoted methane dissociation process on Pt-Al-Ce, which leads to an improved H_2 generation rate and a higher H_2/CO ratio in the produced gas.

3.7 Photo-thermal-driven DRM reaction mechanism on Pt-Al-Ce

Based on the experimental results and *in situ* DRIFTS analyses, a possible DRM reaction

mechanism is proposed. CH_4 dissociation has been widely accepted to take place on Pt reactions sites forming C* and H* intermediates (reactions 1-2), where Pt active sites activate methane and weaken the C-H bonding.[15, 89] Two H* may couple and form H_2 (reaction 3). The reaction mechanism of CO_2 reduction into CO is slightly complicated. CO_2 can react with H* intermediates and form surface formate (reaction 6),[89, 90] which is converted into CO and -OH (reaction 7). The formate intermediates may also react with H* and form CO and H_2O through the RWGS mechanism (reaction 8). CO can also be formed through the direct reduction of CO_2 by oxygen vacancies (V_O) on the catalyst surface (reaction 9). Due to the high oxygen mobility property of CeO_2, C* may be oxidized by CeO_2 lattice oxygen (O_L) and form CO (reaction 10). Bidentate carbonate (b-CO_3^{2-}) was also believed to be active in reacting with C* intermediate and form CO (reaction 11).[91]

The concentrated solar irradiation can additionally promote the DRM performance of Pt-Al-Ce catalyst through the photocatalytic effect. In the photocatalytic process, CeO_2 is excited by photon and generate electrons (e^-) and holes (h^+) (reaction 12). The electrons can reduce the bulk CeO_2 and generate V_O on the catalyst surface (reaction 13), which enhances CO generation. As for methane dissociation, the photoexcited holes can extract H atoms from activated methane molecules on Pt nanoparticles,[92] which facilitates dissociation of CH_x* (reactions 14-15) and leads to promoted H_2 production.

$$CH_4 \rightarrow CH_x^* + (4-x)H^* \quad (1)$$

$$CH \rightarrow C^* + H^* \quad (2)$$

$$2H^* \rightarrow H_2 \quad (3)$$

$$CO_2 + O_L \rightarrow m\text{-}CO_3^{2-} \quad (4)$$

$$m\text{-}CO_3^{2-} \rightarrow b\text{-}CO_3^{2-} \text{ (under excessive } CO_2) \quad (5)$$

$$H^* + CO_2 \rightarrow HCOO\text{-} \quad (6)$$

$HCOO^- \rightarrow CO + {}^-OH$ (7)

$H^* + HCOO^- \rightarrow CO + H_2O$ (8)

$V_O + CO_2 \rightarrow CO + O_L$ (9)

$C^* + O_L \rightarrow CO + V_O$ (10)

$b\text{-}CO_3^{2-} + C^* \rightarrow 2CO + O_L$ (11)

$CeO_2 + h\nu \rightarrow CeO_2 + e^- + h^+$ (12)

$Ce^{4+} + e^- \rightarrow Ce^{3+} + V_O$ (13)

$CH_x^* + h^+ \rightarrow CH_{(1-x)}^* + H^*$ (14)

$CH^* + h^+ \rightarrow C^* + H^*$ (15)

4. Conclusions

In this work, Pt decorated Al_2O_3-CeO_2 catalyst was prepared and applied for photo-thermal driven DRM process. Strong synergy effects were observed on the Pt-Al-Ce catalyst. Investigations revealed the bi-functional characteristics of Al_2O_3-CeO_2 binary substrate: Al_2O_3 stimulates CH_4 dissociation while CeO_2 facilitates CO_2 reduction and coke elimination, leading to remarkable DRM catalyzing efficiency. Pt-Al-Ce catalyst shows a near-unity H_2/CO production ratio, which is likely related to the promoted reactivity and concentrated reaction sites of the Pt nanoparticles on the catalyst, as evidenced by the *in situ* DRIFTS analyses. Concentrated solar irradiation Pt-Al-Ce was found to facilitate reactant activation and reduce the reaction activation energy through the photocatalytic effect of the CeO_2 components, which leads to promoted DRM catalyzing efficiency.

Acknowledgements

The authors gratefully acknowledge the financial supports from U. S. National Science Foundation

(Award #: CBET 1924466 and CBET 1924574). X. Feng is partially supported by the 2020 Graduate Summer Research Grant sponsored by J. Mike Walker ’66 Department of Mechanical Engineering at Texas A&M University. The use of Material Characterization Facilities at Texas A&M University is acknowledged.

References

1. J. R. Rostrup-Nielsen, *Catalysis Today*, 2002, **71**, 243-247.
2. A. Iulianelli, S. Liguori, J. Wilcox and A. Basile, *Catalysis Reviews*, 2016, **58**, 1-35.
3. A. Abdulrasheed, A. A. Jalil, Y. Gambo, M. Ibrahim, H. U. Hambali and M. Y. Shahul Hamid, *Renewable and Sustainable Energy Reviews*, 2019, **108**, 175-193.
4. W.-J. Jang, J.-O. Shim, H.-M. Kim, S.-Y. Yoo and H.-S. Roh, *Catalysis Today*, 2019, **324**, 15-26.
5. Q. Jiang, S. Faraji, D. A. Slade and S. M. Stagg-Williams, in *Membrane Science and Technology*, eds. S. T. Oyama and S. M. Stagg-Williams, Elsevier, 2011, vol. 14, pp. 235-273.
6. H. Huang, M. Mao, Q. Zhang, Y. Li, J. Bai, Y. Yang, M. Zeng and X. Zhao, *Advanced Energy Materials*, 2018, **8**, 1702472.
7. J. K. Adewole, A. L. Ahmad, S. Ismail and C. P. Leo, *International Journal of Greenhouse Gas Control*, 2013, **17**, 46-65.
8. R. Franke, D. Selent and A. Börner, *Chemical Reviews*, 2012, **112**, 5675-5732.
9. Y. Zeng, X. Zhu, D. Mei, B. Ashford and X. Tu, *Catalysis Today*, 2015, **256**, 80-87.
10. J. Lu, C. Zhu, C. Pan, W. Lin, J. P. Lemmon, F. Chen, C. Li and K. Xie, *Science Advances*, 2018, **4**, eaar5100.
11. S. Shoji, A. S. Bin Mohd Najib, M.-W. Yu, T. Yamamoto, S. Yasuhara, A. Yamaguchi, X. Peng,

S. Matsumura, S. Ishii, Y. Cho, T. Fujita, S. Ueda, K.-P. Chen, H. Abe and M. Miyauchi, *Chem Catalysis*, 2021.

12. S. Dasappa, H. V. Sridhar, G. Sridhar, P. J. Paul and H. S. Mukunda, *Biomass and Bioenergy*, 2003, **25**, 637-649.
13. M. Kushida, A. Yamaguchi, Y. Cho, T. Fujita, H. Abe and M. Miyauchi, *ChemPhotoChem*, 2021, **5**, 275-281.
14. F. Pan, X. Xiang, W. Deng, H. Zhao, X. Feng and Y. Li, *ChemCatChem*, 2018, **10**, 940-945.
15. F. Pan, X. Xiang, Z. Du, E. Sarnello, T. Li and Y. Li, *Applied Catalysis B: Environmental*, 2020, **260**, 118189.
16. R. Ma, S. Zhang, T. Wen, P. Gu, L. Li, G. Zhao, F. Niu, Q. Huang, Z. Tang and X. Wang, *Catalysis Today*, 2019, **335**, 20-30.
17. Y. Wang, J. Zhao, T. Wang, Y. Li, X. Li, J. Yin and C. Wang, *Journal of Catalysis*, 2016, **337**, 293-302.
18. P. Li, X. Chen, Y. Li and J. W. Schwank, *Catalysis Today*, 2019, **327**, 90-115.
19. D. Pakhare and J. Spivey, *Chemical Society Reviews*, 2014, **43**, 7813-7837.
20. N. A. K. Aramouni, J. G. Touma, B. A. Tarboush, J. Zeaiter and M. N. Ahmad, *Renewable and Sustainable Energy Reviews*, 2018, **82**, 2570-2585.
21. P. Djinović, I. G. O. Črnivec, J. Batista, J. Levec and A. Pintar, *Chemical Engineering and Processing: Process Intensification*, 2011, **50**, 1054-1062.
22. C. Carrara, J. Múnera, E. A. Lombardo and L. M. Cornaglia, *Topics in Catalysis*, 2008, **51**, 98-106.
23. N. H. Elsayed, N. R. M. Roberts, B. Joseph and J. N. Kuhn, *Applied Catalysis B: Environmental*, 2015, **179**, 213-219.

24. D. Takami, A. Yamamoto and H. Yoshida, *Catalysis Science & Technology*, 2020, **10**, 5811-5814.

25. C. Shi and P. Zhang, *Applied Catalysis B: Environmental*, 2012, **115-116**, 190-200.

26. P. G. Schulz, M. G. Gonzalez, C. E. Quincoces and C. E. Gigola, *Industrial & Engineering Chemistry Research*, 2005, **44**, 9020-9029.

27. S. Damyanova, B. Pawelec, K. Arishtirova, M. V. M. Huerta and J. L. G. Fierro, *Applied Catalysis B: Environmental*, 2009, **89**, 149-159.

28. F. Maleki and G. Pacchioni, *Topics in Catalysis*, 2020, **63**, 1717-1730.

29. I. Wysocka, J. Hupka and A. Rogala, *Catalysts*, 2019, **9**, 540.

30. R. Tang, Z. Zhu, C. Li, M. Xiao, Z. Wu, D. Zhang, C. Zhang, Y. Xiao, M. Chu, A. Genest, G. Rupprechter, L. Zhang, X. Zhang and L. He, *ACS Materials Letters*, 2021, **3**, 1652-1659.

31. R. Benrabaa, A. Löfberg, J. Guerrero Caballero, E. Bordes-Richard, A. Rubbens, R.-N. Vannier, H. Boukhlouf and A. Barama, *Catalysis Communications*, 2015, **58**, 127-131.

32. H. U. Hambali, A. A. Jalil, A. A. Abdulrasheed, T. J. Siang, T. A. T. Abdullah, A. Ahmad and D.-V. N. Vo, *International Journal of Energy Research*, 2020, **44**, 5696-5712.

33. H. Pines and W. O. Haag, *Journal of the American Chemical Society*, 1960, **82**, 2471-2483.

34. D. Zhang, J. Zhang and D. Sun, *Applied Catalysis A: General*, 2020, **606**, 117800.

35. T. Li, L. Zhang, Z. Tao, C. Hu, C. Zhao, F. Yi, X. Gao, X. Wen, Y. Yang and Y. Li, *Fuel*, 2020, **279**, 118487.

36. S. Wu, Y. Li, Q. Zhang, Z. Jiang, Y. Yang, J. Wu and X. Zhao, *Energy & Environmental Science*, 2019, **12**, 2581-2590.

37. S. Wu, Y. Li, Q. Zhang, Q. Hu, J. Wu, C. Zhou and X. Zhao, *Advanced Energy Materials*, 2020, **10**, 2002602.

38. H. Liu, X. Meng, T. D. Dao, H. Zhang, P. Li, K. Chang, T. Wang, M. Li, T. Nagao and J. Ye,

Angewandte Chemie International Edition, 2015, **54**, 11545-11549.

39. H. Liu, T. D. Dao, L. Liu, X. Meng, T. Nagao and J. Ye, *Applied Catalysis B: Environmental*, 2017, **209**, 183-189.
40. G. Zhang, S. Wu, Y. Li and Q. Zhang, *Applied Catalysis B: Environmental*, 2020, **264**, 118544.
41. M. Mao, Q. Zhang, Y. Yang, Y. Li, H. Huang, Z. Jiang, Q. Hu and X. Zhao, *Green Chemistry*, 2018, **20**, 2857-2869.
42. L. Liu, H. Zhao, J. M. Andino and Y. Li, *ACS Catalysis*, 2012, **2**, 1817-1828.
43. B. M. Reddy, K. N. Rao, G. K. Reddy, A. Khan and S.-E. Park, *The Journal of Physical Chemistry C*, 2007, **111**, 18751-18758.
44. S. Boullosa-Eiras, E. Vanhaecke, T. Zhao, D. Chen and A. Holmen, *Catalysis Today*, 2011, **166**, 10-17.
45. L. S. F. Feio, C. E. Hori, S. Damyanova, F. B. Noronha, W. H. Cassinelli, C. M. P. Marques and J. M. C. Bueno, *Applied Catalysis A: General*, 2007, **316**, 107-116.
46. Z. Li and K. Sibudjing, *ChemCatChem*, 2018, **10**, 2994-3001.
47. C. Anandan and P. Bera, *Applied Surface Science*, 2013, **283**, 297-303.
48. C. Lv, C. Zhu, C. Wang, D. Li, X. Ma and D. Yang, *AIP Advances*, 2015, **5**, 037107.
49. R. Murugan, G. Ravi, G. Vijayaprasath, S. Rajendran, M. Thaiyan, M. Nallappan, M. Gopalan and Y. Hayakawa, *Physical Chemistry Chemical Physics*, 2017, **19**, 4396-4404.
50. K. Wang, Y. Chang, L. Lv and Y. Long, *Applied Surface Science*, 2015, **351**, 164-168.
51. M. Li, X. Pan, M. Jiang, Y. Zhang, Y. Tang and G. Fu, *Chemical Engineering Journal*, 2020, **395**, 125160.
52. P. M. A. Sherwood, *Surface Science Spectra*, 1998, **5**, 1-3.
53. J. van den Brand, W. G. Sloof, H. Terryn and J. H. W. de Wit, *Surface and Interface Analysis*,

2004, **36**, 81-88.

54. M. Yang, G. Shen, Q. Wang, K. Deng, M. Liu, Y. Chen, Y. Gong and Z. Wang, *Molecules*, 2021, **26**, 6363.

55. A. Elaziouti, N. Laouedj, A. Bekka and R.-N. Vannier, *Journal of King Saud University - Science*, 2015, **27**, 120-135.

56. R. Singh and R. K. Soni, *Applied Physics A*, 2014, **116**, 689-701.

57. P. Makuła, M. Pacia and W. Macyk, *The Journal of Physical Chemistry Letters*, 2018, **9**, 6814-6817.

58. L. Tao, Y. Shi, Y.-C. Huang, R. Chen, Y. Zhang, J. Huo, Y. Zou, G. Yu, J. Luo, C.-L. Dong and S. Wang, *Nano Energy*, 2018, **53**, 604-612.

59. B. Choudhury, P. Chetri and A. Choudhury, *Journal of Experimental Nanoscience*, 2015, **10**, 103-114.

60. M. Alabdullah, M. Ibrahim, D. Dhawale, J. A. Bau, A. Harale, S. Katikaneni and J. Gascon, *ChemCatChem*, 2021, **13**, 2879-2886.

61. M. Usman, W. M. A. Wan Daud and H. F. Abbas, *Renewable and Sustainable Energy Reviews*, 2015, **45**, 710-744.

62. T. Wang, F. Jiang, G. Liu, L. Zeng, Z.-j. Zhao and J. Gong, *AIChE Journal*, 2016, **62**, 4365-4376.

63. A. Arslan and T. Doğu, *International Journal of Hydrogen Energy*, 2016, **41**, 16752-16761.

64. K. Tomishige, T. Kimura, J. Nishikawa, T. Miyazawa and K. Kunimori, *Catalysis Communications*, 2007, **8**, 1074-1079.

65. L. Yuliati, H. Itoh and H. Yoshida, *Chemical Physics Letters*, 2008, **452**, 178-182.

66. S. Shoji, X. Peng, A. Yamaguchi, R. Watanabe, C. Fukuhara, Y. Cho, T. Yamamoto, S. Matsumura, M.-W. Yu, S. Ishii, T. Fujita, H. Abe and M. Miyauchi, *Nature Catalysis*, 2020, **3**, 148-153.

67. Y. Cho, A. Yamaguchi and M. Miyauchi, *Catalysts*, 2021, **11**, 18.

68. Y. Cho, S. Shoji, A. Yamaguchi, T. Hoshina, T. Fujita, H. Abe and M. Miyauchi, *Chemical Communications*, 2020, **56**, 4611-4614.

69. Z. Du, F. Pan, E. Sarnello, X. Feng, Y. Gang, T. Li and Y. Li, *The Journal of Physical Chemistry C*, 2021, **125**, 18684-18692.

70. D. G. Araiza, A. Gómez-Cortés and G. Díaz, *Catalysis Science & Technology*, 2017, **7**, 5224-5235.

71. G. Jacobs, U. M. Graham, E. Chenu, P. M. Patterson, A. Dozier and B. H. Davis, *Journal of Catalysis*, 2005, **229**, 499-512.

72. L. F. Bobadilla, J. L. Santos, S. Ivanova, J. A. Odriozola and A. Urakawa, *ACS Catalysis*, 2018, **8**, 7455-7467.

73. I. Tankov, W. H. Cassinelli, J. M. C. Bueno, K. Arishtirova and S. Damyanova, *Applied Surface Science*, 2012, **259**, 831-839.

74. A. Yee, S. J. Morrison and H. Idriss, *Journal of Catalysis*, 1999, **186**, 279-295.

75. Z. Hou, X. Zhou, T. Lin, Y. Chen, X. Lai, J. Feng and M. Sun, *New Journal of Chemistry*, 2019, **43**, 5719-5726.

76. L. Liu, C. Zhao, J. Xu and Y. Li, *Applied Catalysis B: Environmental*, 2015, **179**, 489-499.

77. F. Zhao, Z. Liu, W. Xu, S. Yao, A. Kubacka, A. C. Johnston-Peck, S. D. Senanayake, A.-Q. Zhang, E. A. Stach, M. Fernández-García and J. A. Rodriguez, *The Journal of Physical Chemistry C*, 2014, **118**, 2528-2538.

78. P. J. Linstrom, W. G. Mallard and Eds., *NIST Chemistry WebBook, NIST Standard Reference Database Number 69*, National Institute of Standards and Technology, Gaithersburg MD, 20899, 2020.

79. O. Pozdnyakova-Tellinger, D. Teschner, J. Kröhnert, F. C. Jentoft, A. Knop-Gericke, R. Schlögl and A. Wootsch, *The Journal of Physical Chemistry C*, 2007, **111**, 5426-5431.

80. M. J. Kappers, J. T. Miller and D. C. Koningsberger, *The Journal of Physical Chemistry*, 1996, **100**, 3227-3236.

81. O. Pozdnyakova, D. Teschner, A. Wootsch, J. Kröhnert, B. Steinhauer, H. Sauer, L. Toth, F. C. Jentoft, A. Knop-Gericke, Z. Paál and R. Schlögl, *Journal of Catalysis*, 2006, **237**, 1-16.

82. G. Jacobs, L. Williams, U. Graham, D. Sparks and B. H. Davis, *The Journal of Physical Chemistry B*, 2003, **107**, 10398-10404.

83. C. Morterra, A. Zecchina, S. Coluccia and A. Chiorino, *Journal of the Chemical Society, Faraday Transactions 1: Physical Chemistry in Condensed Phases*, 1977, **73**, 1544-1560.

84. J. Szanyi and J. H. Kwak, *Physical Chemistry Chemical Physics*, 2014, **16**, 15117-15125.

85. A. Kaftan, M. Kusche, M. Laurin, P. Wasserscheid and J. Libuda, *Applied Catalysis B: Environmental*, 2017, **201**, 169-181.

86. L. Liu, Y. Jiang, H. Zhao, J. Chen, J. Cheng, K. Yang and Y. Li, *ACS Catalysis*, 2016, **6**, 1097-1108.

87. H. R. Park, A. U. Pawar, U. Pal, T. Zhang and Y. S. Kang, *Nano Energy*, 2021, **79**, 105483.

88. W. Bi, Y. Hu, N. Jiang, L. Zhang, H. Jiang, X. Zhao, C. Wang and C. Li, *Applied Catalysis B: Environmental*, 2020, **269**, 118810.

89. J. Niu, X. Du, J. Ran and R. Wang, *Applied Surface Science*, 2016, **376**, 79-90.

90. X. Su, X. Yang, B. Zhao and Y. Huang, *Journal of Energy Chemistry*, 2017, **26**, 854-867.

91. X. Li, Z.-J. Zhao, L. Zeng, J. Zhao, H. Tian, S. Chen, K. Li, S. Sang and J. Gong, *Chemical Science*, 2018, **9**, 3426-3437.

92. Q. Li, Y. Ouyang, H. Li, L. Wang and J. Zeng, *Angewandte Chemie International Edition*, 2021,

61, e202108069.